Precision manufacturing of glass dielectric resonator antennas for sub-THz applications using laser induced deep etching technology

Elizabeth Bekker,[1,✉] Jiexi Yin,[1] Luca Valenziano,[1] Michael Lootze,[2] Malte Schulz-Ruhtenberg,[2] Thomas Zwick,[1] and Akanksha Bhutani[1]

[1] *Institute of Radio Frequency Engineering and Electronics (IHE), Karlsruhe Institute of Technology, Karlsruhe, Germany*

[2] *GDI, EDE, LPKF Laser & Electronics AG, Garbsen, Germany*

✉ E-mail: elizabeth.bekker@kit.edu

This letter demonstrates for the first time how laser induced deep etching (LIDE) technology is used to manufacture highly precise glass dielectric resonator antenna (DRA) for sub-THz applications. The glass resonator antennas shown in this letter operate in the 110–170 GHz (D-band) frequency range, which is highest frequency at which glass dielectric resonator antennas have been demonstrated to date. The letter discusses the design, manufacturing precision and measurement details for both a single rectangular DRA element, as well as a 4-by-4 array. The measured bandwidth of the singular rectangular DRA stretches from 117–160 GHz, with a peak gain of 6.1 dBi. The array, in turn, has a measured bandwidth of 135–146 GHz, with a peak gain of 13.2 dBi. The excellent measurement results are proof of the suitability of the LIDE technology for highly precise sub-THz antennas.

Introduction: Dielectric resonator antennas (DRAs) have attracted considerable interest in millimetre-wave and terahertz applications owing to their excellent antenna efficiency, wideband characteristics, and integration compatibility with silicon-based semiconductors. Various methods have been developed to realize DRAs in the millimetre-wave band, utilizing materials such as ceramics [1], polymer-ceramic composites [2], high-resistivity silicon [3], and glass [4].

Glass-based dielectric resonator antennas (DRAs) is a growing topic of interest, due to their diverse and advantageous characteristics. The impedance bandwidth of a DRA is inversely related to its relative permittivity [5]. With a typical relative permittivity of approximately 4, glass-based DRAs are inherently suitable for broadband applications. The low permittivity also results in antennas with large opening angles. Thereby, glass DRAs are well-positioned to meet the demands of the next-generation mobile communication systems requiring high data rates and multi-point communication. Furthermore, glass offers exceptional dielectric performance with low loss characteristics, extending well into the sub-terahertz frequency range. Its material advantages include high coplanarity, customizable coefficients of thermal expansion (CTE), high-temperature resilience, and exceptional reliability, positioning it as a compelling choice for cutting-edge antenna designs [6].

Notable examples include transparent DRAs made from K-9 glass, which combine high performance with aesthetic appeal, as discussed in [4–7]. A tri-band glass DRA has also been proposed for Wi-Fi applications, operating at 2.4, 5.2, and 5.8 GHz [8]. A compact, dual band DRA is designed with a high dielectric and low-loss transparent glass material for WLAN in the 5 GHz band in [9]. The optical transparency of the glass antennas opens opportunities for seamless integration into various optical applications, such as forming part of mirrors [10], light covers [11], or even focusing lenses for underlying solar cells [12]. However, due to challenges in fabrication and antenna assembly, glass-based DRAs found in the literature have been limited to frequencies well below 100 GHz. Despite these challenges, the multitude advantages glass substrates offer, make it an attractive material for antennas and packaging applications in the millimetre wave range. For instance, a compact through-glass via (TGV) structure has also been integrated for millimetre-wave wireless chip-to-chip (C2C) communication in 3D system-in-package (SiP) designs at 62 GHz [13]. Additionally, a glass-based miniaturized quasi-Yagi antenna array with an operational bandwidth of 110–170 GHz has been demonstrated in [14]. A high-gain millimetre-wave antenna-in-package (AiP) operating at 150 GHz has been developed using laser induced deep etching (LIDE) technology in [15]. These studies highlight the potential of glass for next-generation high-efficiency, wideband, and compact millimetre-wave antennas. However, the focus falls on glass as a substrate, with limited exploration of its application in DRAs at frequencies above 100 GHz. In this paper, we introduce a novel approach to realizing glass DRAs at the D-band, leveraging LIDE technology.

LIDE is a technique for fabricating intricate microstructures in glass by combining laser irradiation with chemical etching. During the process, a pulsed laser selectively modifies the glass surface, altering its structure locally. These modified regions become more susceptible to chemical etching (typically using hydrofluoric acid) than the surrounding, unaltered glass - enabling the creation of clean and accurate etch profiles. By fine-tuning laser parameters (e.g. wavelength, pulse duration, intensity) and etching time, the depth and shape of the features can be precisely controlled. With LIDE it is possible to produce structures with micrometre-scale accuracy, to fabricate complex geometries like through-holes with a high aspect ratio and cavities, and the process produces minimal stress or cracking compared to mechanical methods, preserving the glass's mechanical and optical properties [16]. This efficient, cost-effective process is particularly well-suited for producing antennas and packaging for sub-THz applications, making it indispensable for next-generation communication systems.

This work demonstrates the use of LIDE technology for highly-precise antennas for sub-THz applications, by way of the design, fabrication and measurement of two antenna prototypes—a singular rectangular DRA (RDRA), and a 4-by-4 RDRA array. To the best of the authors' knowledge, this is the first instance of using LIDE technology to manufacture glass DRAs for sub-THz frequencies, as well as the first demonstration of glass DRAs being fabricated for frequencies above 60 GHz. The paper provides an in-depth discussion of specific details required in the manufacturing process for these glass DRAs, with a detailed evaluation of their fabrication precision through various measurement techniques. This new fabrication method provides a viable pathway for advancing glass DRAs at sub-THz frequencies.

Rectangular dielectric resonator: All borosilicate, alkali-free and fused silica glass types can be used in the LIDE process, but for this design, Schott Borofloat 33 glass (BF33) was chosen as material for the DRA, as it is readily available and low cost. BF33 also exhibits excellent properties for RF applications, such as a low loss tangent ($\tan\delta = 0.008$ at 140 GHz) and a very low surface roughness [15]. The initial glass wafer thickness is 500 μm, but reduces to approximately 460 μm after the chemical etching process. Therefore, the DRA height is established as 460 μm, but its width and length can be chosen freely. By solving the transcendental equations given in [17], the resonant frequency f_{mn} of the $TE^{x}_{\delta mn}$ mode of the RDRA can be calculated. For a RDRA of length 850 μm and width 438 μm, the resonant frequency of the $TE^{x}_{\delta 11}$ mode is calculated as 140 GHz. The RDRA is fed with a slot-coupled microstrip feed. The length of the slot is chosen to be approximately $\lambda/2$ at 125 GHz. A probe-based antenna measurement setup is used to characterize the antenna. Probe-based measurements in D-band take place with single-ended (GSG) probes, therefore a transition from microstrip to a grounded coplanar waveguide (GCPW), with a characteristic impedance of 50 Ω, is required. The design of the transition is described in detail in [18]. The feed substrate was chosen as fused silica, with a 3 μm gold layer. Figure 1 shows the simulation model of the RDRA with relevant parameters, and the E-field distribution of the $TE^{x}_{\delta 11}$ mode at 140 GHz.

To reduce unwanted radiation from the microstrip feed line, a row of mushroom electromagnetic bandgap (MEBG) unit cells are placed at the edge of the feed substrate. The MEBG operates as a high-impedance surface over specific frequency ranges, referred to as surface wave bandgaps. Its structure consists of a metal patch linked to the ground plane through a centrally placed vertical via. The characteristics of the MEBG unit cells are analysed by simulating their dispersion diagram using the Eigenmode solver of the 3D EM analysis software CST Studio Suite. From Figure 2 it can be seen that a surface wave bandgap exists between 114–155 GHz. The MEBG improves the front-to-back-ratio of the antenna by 4 dB. The dimensions of the RDRA and feed are optimized with CST Studio Suite. The final dimensions are listed in Table 1. The total simulated efficiency of the RDRA is 90%.

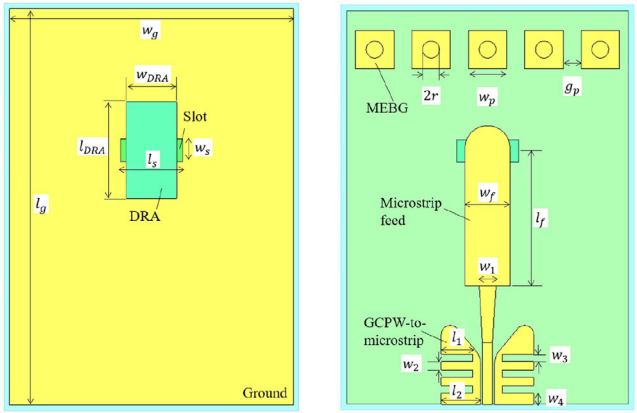

Fig. 1 *Simulation model of RDRA with relevant parameters: (a) Antenna view; (b) Feed view; (c) E-field distribution of the* $TE^{x}_{\delta 11}$ *mode at 140 GHz*

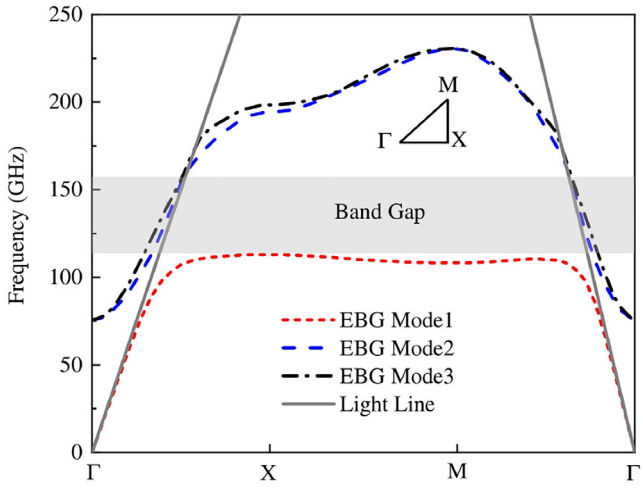

Fig. 2 *Dispersion diagram of the MEBG unit cell*

Table 1. Dimensions of RDRA and accompanying feed substrate (all dimensions are in μm*)*

Parameter	Value	Parameter	Value	Parameter	Value
w_g	2500	r	75	l_1	280
l_g	3500	w_p	340	w_2	75
w_{DRA}	440	g_p	160	l_2	350
l_{DRA}	850	w_f	400	w_3	65
l_s	550	l_f	1200	w_4	100
w_s	200	w_1	150		

4-by-4 dielectric resonator array: After the performance of the DRA element was verified, a 4-by-4 array is designed. The antenna spacing between neighbouring elements is chosen as λ/2 at 140 GHz. Similar to the single-element design, the energy is coupled to the DRA through a slot, with a microstrip-based feeding network. To distribute power efficiently across the array, a one-to-sixteen power divider is designed. The power divider incorporates a quarter-wavelength transformer, in different sections of the feeding network, with an impedance of 90 Ω, to facilitate the transition to the 64 Ω microstrip line at the antenna. The dimensions of the DRAs and the microstrip lines are optimized to enhance the impedance bandwidth and gain of the array. The height of the DRAs are maintained from the single-element design, as it is determined by the wafer thickness.

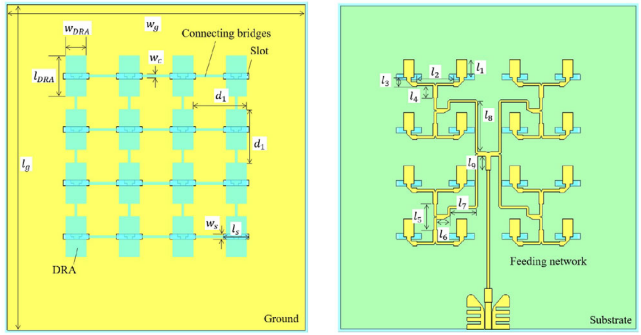

Fig. 3 *Simulation model of 4-by-4 array with relevant parameters*

Table 2. Dimensions of 4-by-4 array and accompanying feed substrate (all dimensions are in μm*)*

Parameter	Value	Parameter	Value	Parameter	Value
w_g	6000	w_c	50	l_5	522
l_g	6550	d_1	1075	l_6	276.50
w_{DRA}	419	l_1	361.75	l_7	524
l_{DRA}	817	l_2	746.50	l_8	1012.50
w_s	114	l_3	188.25	l_9	276.50
l_s	520	l_4	252		

A notable challenge which complicates the assembly process of large scale DRA arrays, is the placement of individual DRA elements within the desired accuracy. In order to address this issue, in this design, support bridges are introduced to connect all 16 elements into a unified structure; significantly reducing the assembly effort. Leveraging the high precision, and lack of propagating cracks, LIDE technology is known for, the glass bridges are designed with a width as narrow as 50 μm. Simulation results confirm that the influence of such a thin bridge on the array's performance is negligible. This support bridge significantly simplifies the assembly process. The final model of the array, along with its key parameters, is shown in Figure 3, with the dimensions summarized in Table 2. The simulated loss of the feeding network is 2.3 dB. The total simulated efficiency of the array is 84%.

Manufacturing of glass antenna samples: The glass antenna prototypes are manufactured by LPKF. During the chemical etching process, the DRA needs to remain attached to the wafer. If the DRA is completely separated from the glass wafer during the etching process, the DRA itself will fall into the etchant and continue to etch away. As the DRAs are very small and also transparent, they will be very difficult to locate in the etching liquid if they were to separate from the wafer. Therefore, a support bridge that connects the DRA to the glass wafer should be chosen with care. The support should satisfy several requirements: firstly, it should be strong enough that the DRAs do not separate during the etching process and survive transportation to other facilities for assembly; further, it should be possible to break the DRAs from the wafer, without significant damage to the DRA, the neighbouring DRAs or the glass wafer; and lastly, the piece of the support bridges that remain after breaking the DRA from the wafer, should not interfere with the DRA's performance.

Placing the support bridges on the longer edge of the DRA ensures that any remnants of the support bridges that remain after breakout have very little influence on the electric field distribution of the $TE^{x}_{\delta 11}$ mode. Figure 4 shows the four different attachment variants that are evaluated in this letter. For Type 1, two support bridges, with a width and length of 100 μm, are used to secure the RDRA to the glass wafer. Types 2 and 3

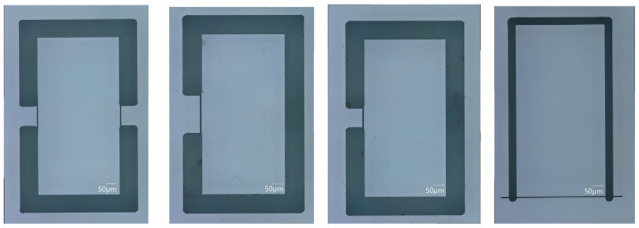

Fig. 4 *Attachment types: (a) Type 1; (b) Type 2; (c) Type 3; (d) Type 4*

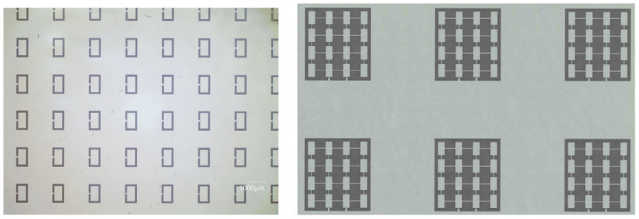

Fig. 5 *Section of glass wafer showing multiple intact samples: (a) singular RDRAs; (b) RDRA arrays*

Fig. 6 *Remnants of the broken support bridges for different attachment types: (a) Type 2; (b) Type 3; (c) Type 4*

are similar, with only a single bridge holding the DRA to its wafer; the bridges are 100 μm wide, and 200 μm and 100 μm long, respectively. For Type 4, a different approach is tested, with the short side of the RDRA remaining attached. However, a single row of laser pulses are used to make a cut approximately half-way through the wafer thickness, weakening the glass locally, and facilitating the DRA's removal.

All supports are successful in preventing the DRAs from disappearing into the etchant—no DRAs are separated from the wafer during the etching process (see Figure 5a as example). To test the breakout yield, a plastic tip tweezers or fine tip cotton swab is used to gently apply pressure to the DRA in the wafer, to break it apart from its support bridges. It was determined that it was very challenging to remove the DRAs with the double support bridges (Type 1) from the wafer, without shattering the DRAs, or the surrounding wafer. The force required to break the DRA from the wafer was much larger than the maximum force the DRA could withstand without shattering, and as such, no DRAs using the Type 1 attachment, could be removed from the wafer without cracks or chips forming in the DRA and surrounding wafer. As the breakout yield of this method is very low, the double support structure is not recommended for future applications. For Types 2 to 4, all supporting bridges are easily separated, with all attachment types resulting in a 100% breakout yield. As the LIDE process has been well-established prior, but is used for the first time to produce highly-precise antennas in this paper, the successful separation of the antennas from the surrounding wafer is the primary indicator of the overall yield rate of the process. As such the breakout yield determines the overall yield rate. At least 600 individual antenna elements can be obtained in this manner, from a singular wafer with a 100 mm diameter.

In Figure 6 the remnants of the broken support bridges for attachment Types 2 to 4, are shown. The breakout remnants of Types 2 and 3 are right-angled triangles, with a base approximately 100 μm in width, and 200 μm and 100 μm long, respectively. In Figure 6c, the short edge of the DRA appears smoother than the longer edge. This is an indication

Table 3. Minimum, maximum, average and MAE of RDRA and 4-by-4 array dimensions (all dimensions are in μm*)*

Antenna	Parameter	Min.	Max.	Ave.	MAE
Single RDRA	w_{DRA}	437.71	443.30	440.29	1.53
	l_{DRA}	847.33	854.25	850.66	2.11
	h_{DRA}	462.65	466.46	464.41	4.87
4-by-4 RDRA array	w_{DRA}	417.81	421.39	419.36	0.71
	l_{DRA}	814.68	818.43	816.37	0.87
	h_{DRA}	461.64	466.16	464.16	4.16
	w_c	49.01	52.52	50.14	0.83
	d_1	1074.01	1076.73	1075.27	0.63

of where the DRA, with the Type 4 attachment, separated from the wafer. Updated simulation models of the RDRA, to include breakout remnants similar to what can be seen in Figure 6, shows that the breakout remnants have negligible impact on the gain, reflection and radiation patterns, as expected. While none of the breakout remnants have any significant influence on the antenna's performance, Type 4 is recommended for future use for singular DRAs where possible, as a negligible amount of the support bridge remains after breakout. In the case where Type 4 is not possible, for example with more complex shapes, such as circular or pyramidal DRAs, or arrays, Type 3 is recommended. Therefore, for the 4-by-4 array, two narrow bridges are used to connect the array to the glass wafer during production—see Figure 5b. The bridges are 120 μm in width.

Table 3 summarizes the minimum, maximum, average and mean absolute error (MAE) of the relevant parameters, for the RDRA and 4-by-4 array. The accuracy of the manufactured samples are quantified by measuring the relevant dimensions with a Keyence VHX digital microscope, with a minimum magnification of 150×. The width and length of 50 RDRA samples are measured—the samples are chosen at random across two different wafers, from different attachment types. As for the array samples, 5 different arrays are chosen at random across the wafer, and 4 individual elements are measured per array, resulting in a total of 20 measurements. The height of 10 RDRAs and 10 arrays are measured to determine the height accuracy. As expected, the DRA prototypes that are manufactured with the LIDE process, exhibit excellent accuracy, with an MAE of the transversal dimensions of the array prototypes <1 μm. The MAE of the height is the highest, since that is the most difficult parameter to control as the etching time, etchant and glass type all influence the resultant wafer thickness. Nevertheless, the MAE of the height is still <5 μm.

Assembly of prototypes: The feed substrates for both antennas are fabricated with the thin-film process from applied thin-film products (ATP). The antennas are subsequently assembled at the IHE, using the Finetech Fineplacer Pico. A layer of die attach film, AFT102 from Furukawa Electric [19], with a thickness of 10 μm, is used to attach the DRAs to their feed substrates. Microscope images of assembled prototypes of the single RDRA, and the 4-by-4 RDRA array, can be seen in Figure 7.

Measurements and results: The antennas are characterized using a probe-based antenna measurement setup. A detailed description of the antenna measurement station, the measurement procedure and limitations, can be found in [20]. The antennas are placed on a 3D printed frame, on which a thin piece of Rohacell 31, a polymethacrylimide (PMI) based structural foam, from EVONIK, is glued. The Rohacell support plate closely approximates air, with a relative permittivity of 1.04, and therefore, has a negligible influence on the antenna under test (AUT) performance. The probe pads (formed with the GCPW-to-microstrip transition), and the radiation direction of the antennas, are in opposite directions, thus, a small opening, the approximate size of the AUT, is made in the Rohacell support. The assembled prototypes are placed atop the Rohacell, with the DRAs centred in the opening and facing downwards. Subsequently, the feed substrate is supported around the edges by the Rohacell—this prevents the feed substrate from tipping from force due to the probing. Figure 8 shows a cross section of a model of the

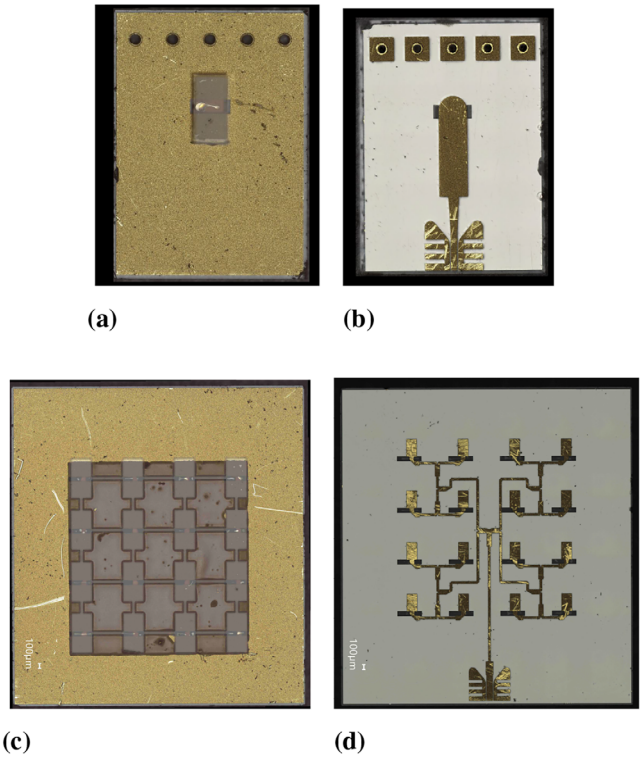

Fig. 7 *Assembled samples: (a) Singular RDRA: Antenna view; (b) Singular RDRA: Feed view; (c) 4-by-4 RDRA array: Antenna view; (d) 4-by-4 RDRA array: Feed view*

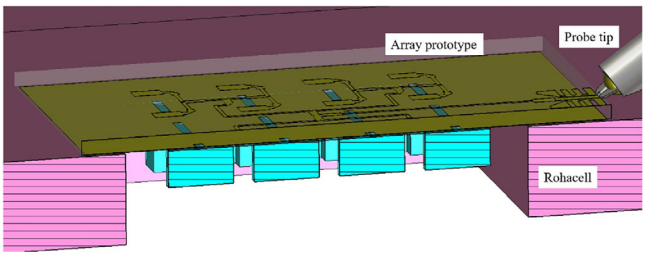

Fig. 8 *Cross section of visualization of Rohacell support plate, an assembled array sample and the probe tip*

Rohacell support, the array and the probe, for easier visualization of the aforementioned description.

The measurement results for the singular RDRA and the 4-by-4 array can be seen in Figures 9 and 10, respectively. Overall, for both the RDRA and the 4-by-4 array, there is an excellent agreement between simulation and measurement. The resonances of the measured return loss in Figure 9a are shifted by only 6 GHz in comparison with the simulation. The measured reflection coefficient of the RDRA is below −10 dB between 117–160 GHz (a relative bandwidth of 31%). As for the RDRA gain measurement, the measured and simulated gain differ by a maximum of 1 dB, with a peak gain of 6.1 dBi at 140 GHz. There are negligible differences between the simulation and measurement for both the E- and H-plane radiation patterns as well. Note that pattern measurements are limited to the hemisphere where the antenna radiates away from the probe (see Figure 8), since measurements of the back lobes are influenced by probe radiation [21], as well as reflections from the support structures of the frequency extension modules. The E-plane measurement range is further limited to an angular range of approximately 30° due to the support structures of the setup [20].

The array exhibits a measured reflection coefficient below −10 dB from 135–146 GHz and peak gain of 13.2 dBi, at 137 GHz. The measured and simulated gain differ by a maximum of 1.3 dB. The difference between the measured and simulated gain can be contributed to constructive interference due to multipath reflections off of the metal support structures of the antenna measurement setup, probe radiation,

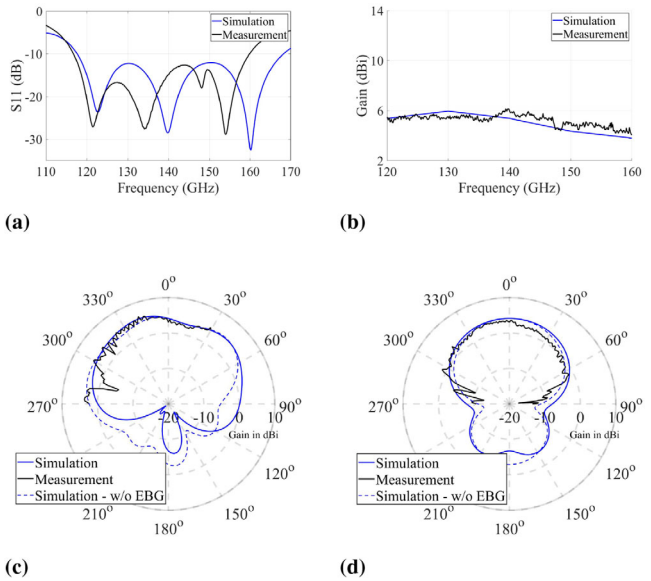

Fig. 9 *Measurement and simulation results of RDRA: (a) Reflection coefficient; (b) Realized gain; (c) E-plane pattern; (d) H-plane pattern*

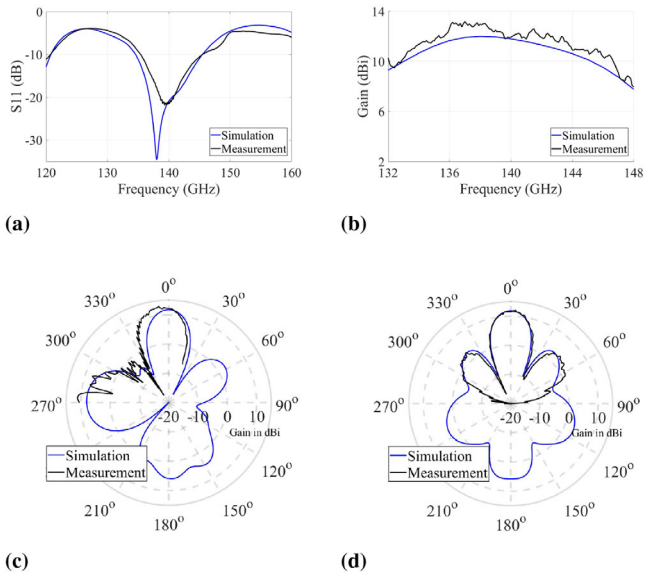

Fig. 10 *Measurement and simulation results of 4-by-4 array: (a) Reflection coefficient; (b) Realized gain; (c) E-plane pattern; (d) H-plane pattern*

or slight deviations in the error terms originating during the probe calibration. While the individual antenna element demonstrates broadband performance, two factors contribute to a reduction in the array's bandwidth. First, the quarter-wavelength transformers used in the power divider. Second, the closely spaced DRAs result in a mutual coupling of 8.1 dB between neighbouring elements in the same row. The mutual coupling causes impedance mismatches, further narrowing the array's impedance bandwidth. A slight tilt can be noticed in the E-plane radiation pattern. As the probe applies pressure at the one edge of the feed substrate, the Rohacell directly underneath is slightly compressed. As a result, the opposite edge of the feed substrate is lifted into air and the assembled sample is slightly tilted and no longer completely planar, radiating away from boresight.

Conclusion: The singular RDRA shown in this work, achieves a measured bandwidth of 117–160 GHz with a peak gain of 6.1 dBi, while the array delivers a bandwidth of 135–146 GHz with a peak gain of 13.2 dBi. In Table 4, the DRAs demonstrated in this work are compared to state-of-the-art DRAs and arrays operating in the 110–170 GHz (D-band) frequency range. Few examples of DRAs or DRA arrays above 110 GHz, particularly in D-band, are reported in the literature. In

Table 4. State-of-the-art DR antennas and antenna arrays in D-band

	Ref.	Antenna description	Freq. (GHz)	Relative bandwidth	Peak gain (dBi)
Singular DRA	[1]	Alumina cube on Megtron 5680 (N) substrate	115–162	34%	5.5
	[22]	Alumina RDRA in a surface mount short horn, on Alumina substrate	119–170	35%	9.5
	[23]	On-chip 3D-printed alumina with feed in SiGe BiCMOS BEOL	138–158	14%	4.3
	[24]	On-chip alumina DRA with higher order mode	128–138	8%	7.5
	This work	BF33 RDRA made with LIDE, on fused silica substrate	117–160	31%	6.1
DRA array	[25]	1×2 on-chip alumina DRA array with series-fed, stacked elements	123–137	11%	4.7
	[26]	1×4 on-chip alumina DRA array with half-mode cavity feed	120–140	15%	8.2
	This work	4×4 BF33 RDRA array made with LIDE, on fused silica substrate	135–146	8%	13.2

comparison with the other alumina-based DRAs in the table, which have a relative permittivity approximately 2.5 times higher than glass, glass resonators enable broader bandwidths and wider opening angles, albeit with a more moderate gain. The presented singular RDRA achieves one of the highest relative bandwidths and exhibits a competitive peak gain.

The proposed DRA array stands out as the largest array in D-band, and subsequently delivers the highest gain. The LIDE process facilitates the inclusion of thin support bridges between adjacent elements, minimizing impact on the radiation pattern while significantly simplifying and enhancing the accuracy of the assembly of the array. This capability of LIDE technology enables precise, efficient fabrication of large arrays, making it a promising solution for scalable antenna manufacturing, particularly for advanced 6G MIMO systems. This study marks a definite advancement in sub-THz antenna technology by demonstrating the use of LIDE technology for the precise fabrication of glass DRAs. A detailed exploration of manufacturing processes and evaluation of fabrication precision is presented here. Furthermore, this is also the first reported application of glass DRAs at frequencies exceeding 60 GHz.

Author contributions: **Elizabeth Bekker**: Conceptualization; formal analysis; investigation; methodology; validation; visualization; writing—original draft; writing—review and editing. **Jiexi Yin**: Funding acquisition; investigation; methodology; writing—original draft. **Luca Valenziano**: Methodology. **Michael Lootze**: Conceptualization; investigation; methodology; resources. **Malte Schulz-Ruhtenberg**: Project administration; resources; writing—review and editing. **Thomas Zwick**: Funding acquisition; resources; supervision. **Akanksha Bhutani**: Conceptualization; funding acquisition; project administration; supervision; writing—review and editing.

Acknowledgements: This work is supported financially by the Federal Ministry of Education and Research of Germany, through the project ESSENCE (grant number: 16KISK173) and through the project Open6GHub (grant number: 16KISK010). Jiexi Yin acknowledges support as a fellow of the Young Investigator Group Preparation Program funded jointly via the University of Excellence strategic fund at the Karlsruhe Institute of Technology (administered by the federal government of Germany) and the Ministry of Science, Research and Arts of Baden-Württemberg (Germany).

Conflict of interest statement: The authors declare no conflicts of interest.

Data availability statement: Data available on request from the authors.

Received: *4 December 2024* Accepted: *3 January 2025*
doi: 10.1049/ell2.70141

References

1 Li, T., et al.: Design of wideband dielectric resonator antenna for D-band applications. In: *2021 International Symposium on Antennas and Propagation (ISAP)*, pp. 1–2. IEEE, Piscataway, NJ (2021)
2 Luo, W., et al.: High gain dielectric resonance antenna array for millimeter wave vehicular wireless communication. Progress Electromagn. Res. C **108**, 63–78
3 Bashir, M.F., Wietstruck, M.: Design and investigation of 2x2 dielectric resonator antennas array for sub-thz applications. In: *2024 18th European Conference on Antennas and Propagation (EuCAP)*, pp. 1–4. IEEE, Piscataway, NJ (2024)
4 Fang, X.S., Leung, K.W.: Aesthetic transparent dielectric resonator antenna with omnidirectional radiation pattern. In: Proceedings of the 2012 IEEE International Symposium on Antennas and Propagation, pp. 1–2. IEEE, Piscataway, NJ (2012)
5 Keyrouz, S., Caratelli, D.: Dielectric resonator antennas: basic concepts, design guidelines, and recent developments at millimeter-wave frequencies. *Int. J. Antennas Propag.* **2016**, 1–20 (2016). https://doi.org/10.1155/2016/6075680
6 Chaloun, T., et al.: RF glass technology is going mainstream: review and future applications. *IEEE J. Microwaves* **3**(2), 783–799 (2023). https://doi.org/10.1109/JMW.2023.3256413
7 Fang, X.S., Chen, S.M.: Design of the wide dual-band rectangular souvenir dielectric resonator antenna. *IEEE Access* **7**, 161621–161629 (2019). https://doi.org/10.1109/ACCESS.2019.2951819
8 Hu, P.F., et al.: Diversity glass antennas for tri-band WiFi applications. *Engineering* **23**, 157–169 (2023). https://doi.org/10.1016/j.eng.2022.09.011
9 Mehmood, A., et al.: Dual band dielectric resonator antenna for Hiperlan based on transparent glass material. In: GeMiC 2014; German Microwave Conference, pp. 1–4. IEEE, Piscataway, NJ (2014)
10 Yang, N., Leung, K.W., Lim, E.H.: Mirror-integrated dielectric resonator antenna. *IEEE Trans. Antennas Propag.* **62**(1), 27–32 (2014). https://doi.org/10.1109/TAP.2013.2287007
11 Leung, K.W., et al.: Dual-function radiating glass for antennas and light covers–part i: omnidirectional glass dielectric resonator antennas. *IEEE Trans. Antennas Propag.* **61**(2), 578–586 (2013). https://doi.org/10.1109/TAP.2012.2216495
12 Lim, E.H., Leung, K.W.: Transparent dielectric resonator antennas for optical applications. *IEEE Trans. Antennas Propag.* **58**(4), 1054–1059 (2010). https://doi.org/10.1109/TAP.2010.2041315
13 Hwangbo, S., Yoon, Y.K., Shorey, A.B.: Millimeter-wave wireless chip-to-chip (C2C) communications in 3D system-in-packaging (SIP) using compact through glass via (TGV)-integrated antennas. In: 2018 IEEE 68th Electronic Components and Technology Conference (ECTC), pp. 2074–2079. IEEE, Piscataway, NJ (2018)
14 Erdogan, S., et al.: D-band integrated and miniaturized quasi-Yagi antenna array in glass interposer. *IEEE Trans. Terahertz Sci. Technol.* **13**(3), 270–279 (2023). https://doi.org/10.1109/TTHZ.2023.3242224
15 Galler, T., et al.: Glass package for radar MMICs above 150 GHz. *IEEE J. Microwaves* **2**(1), 97–107 (2022). https://doi.org/10.1109/JMW.2021.3122067
16 Santos, R., et al.: Bringing new life to glass for wafer-level packaging applications. In: 2020 International Wafer Level Packaging Conference (IWLPC), pp. 1–7. IEEE, Piscataway, NJ (2020)
17 Petosa, A., Thirakoune, S.: Rectangular dielectric resonator antennas with enhanced gain. *IEEE Trans. Antennas Propag.* **59**(4), 1385–1389 (2011). https://doi.org/10.1109/TAP.2011.2109690

18 Bekker, E., et al.: Broadband, cia-less grounded coplanar waveguide-to-m transition in D-band. In: 2023 53rd European Microwave Conference (EuMC), pp. 528–531. IEEE, Piscataway, NJ (2023)
19 Furukawa Electric: electrically/thermally conductive dicing die attach film. https://www.furukawa.co.jp/uvtape/en/technology/cdaf.html (2023). Accessed 01 Oct 2023
20 Beer, S., Zwick, T.: Probe based radiation pattern measurements for highly integrated millimeter-wave antennas. In: Proceedings of the Fourth European Conference on Antennas and Propagation, pp. 1–5. IEEE, Piscataway, NJ (2010)
21 Hebeler, J., Zwick, T., Bhutani, A.: Radiation behaviour of mm-wave on-wafer probes in H-band and the influence on antenna measurements. *Electron. Lett.* **60**(3), e13116 (2024). https://doi.org/10.1049/ell2.13116
22 Bekker, E., et al.: Wideband, high gain dielectric resonator antenna in embedded surface mount short horn in D-band. In: 2023 53rd European Microwave Conference (EuMC), pp. 86–89. IEEE, Piscataway, NJ (2023)
23 Haag, A., et al.: Efficient D-band on-chip antennas in silicon germanium technologies. In: 2024 54th European Microwave Conference (EuMC), pp. 888–891. IEEE, Piscataway, NJ (2024)
24 Hou, D., et al.: D-band on-chip higher-order-mode dielectric-resonator antennas fed by half-mode cavity in CMOS technology. *IEEE Antennas Propag. Mag.* **56**(3), 80–89 (2014). https://doi.org/10.1109/MAP.2014.6867684
25 Hou, D., et al.: 130-GHz on-chip meander slot antennas with stacked dielectric resonators in standard CMOS technology. *IEEE Trans. Antennas Propag.* **60**(9), 4102–4109 (2012). https://doi.org/10.1109/TAP.2012.2207077
26 Hou, D., et al.: 130 GHz on-chip dielectric resonator antenna array in CMOS technology. In: 2017 Sixth Asia-Pacific Conference on Antennas and Propagation (APCAP), pp. 1–3. IEEE, Piscataway, NJ (2017)